The Equatorial Pacific Cold Tongue Bias in CESM1 and Its Influence on ENSO Forecasts

XIAN WU,[a] YUKO M. OKUMURA,[b] PEDRO N. DINEZIO,[c] STEPHEN G. YEAGER,[a] AND CLARA DESER[a]

[a] *Climate and Global Dynamics Division, National Center for Atmospheric Research, Boulder, Colorado*
[b] *Institute for Geophysics, Jackson School of Geosciences, The University of Texas at Austin, Austin, Texas*
[c] *Department of Atmospheric and Oceanic Sciences, University of Colorado Boulder, Boulder, Colorado*

(Manuscript received 21 June 2021, in final form 24 January 2022)

ABSTRACT: The mean-state bias and the associated forecast errors of the El Niño–Southern Oscillation (ENSO) are investigated in a suite of 2-yr-lead retrospective forecasts conducted with the Community Earth System Model, version 1, for 1954–2015. The equatorial Pacific cold tongue in the forecasts is too strong and extends excessively westward due to a combination of the model's inherent climatological bias, initialization imbalance, and errors in initial ocean data. The forecasts show a stronger cold tongue bias in the first year than that inherent to the model due to the imbalance between initial subsurface oceanic states and model dynamics. The cold tongue bias affects not only the pattern and amplitude but also the duration of ENSO in the forecasts by altering ocean–atmosphere feedbacks. The predicted sea surface temperature anomalies related to ENSO extend to the far western equatorial Pacific during boreal summer when the cold tongue bias is strong, and the predicted ENSO anomalies are too weak in the central-eastern equatorial Pacific. The forecast errors of pattern and amplitude subsequently lead to errors in ENSO phase transition by affecting the amplitude of the negative thermocline feedback in the equatorial Pacific and tropical interbasin adjustments during the mature phase of ENSO. These ENSO forecast errors further degrade the predictions of wintertime atmospheric teleconnections, land surface air temperature, and rainfall anomalies over the Northern Hemisphere. These mean-state and ENSO forecast biases are more pronounced in forecasts initialized in boreal spring–summer than other seasons due to the seasonal intensification of the Bjerknes feedback.

KEYWORDS: Pacific Ocean; ENSO; Seasonal forecasting; Model errors

1. Introduction

The tropical Pacific Ocean exhibits zonal contrast in mean sea surface temperature (SST) between the western warm pool and the eastern equatorial cold tongue. The eastern equatorial Pacific cold tongue controls climatological SST and rainfall patterns across a large area of the tropics. The cold tongue simulated by the successive generations of Coupled Model Intercomparison Project (CMIP) models is commonly too cold and extends excessively westward compared to observations (Mechoso et al. 1995; Davey et al. 2002; Zheng et al. 2012; Brown et al. 2014; Bellenger et al. 2014; Planton et al. 2020; Guilyardi et al. 2020; Jiang et al. 2021). This cold tongue SST bias in models has been attributed to the misrepresentations of dynamic and thermodynamic processes in the equatorial Pacific, including too strong equatorial zonal surface winds, too strong oceanic horizontal and vertical temperature advection, too little SST damping due to erroneously positive cloud–shortwave radiation feedback, and misrepresentations of subseasonal variability, such as tropical instability waves (Mechoso et al. 1995; Davey et al. 2002; Wittenberg et al. 2006; Zheng et al. 2012; Vannière et al. 2013; Ray et al. 2018; Siongco et al. 2020). The cold tongue SST bias in coupled models is also related to the bias of the intertropical convergence zone (ITCZ) simulated in atmospheric models, which influences the surface wind bias in the equatorial Pacific (Lin 2007; de Szoeke and Xie 2008; Li and Xie 2014). Besides the annual mean bias, most CMIP5 models erroneously simulate the timing and amplitude of the annual cycle of the eastern equatorial Pacific SSTs (e.g., Chen and Jin 2017; Wengel et al. 2019).

The climatological cold tongue bias has been suggested to affect the simulations of tropical climate variations, especially the leading mode of interannual climate variability—El Niño–Southern Oscillation (ENSO). In association with the westward extension of the cold tongue, equatorial SST, surface wind, and precipitation variations related to ENSO events are shifted too far west in climate models compared to observations (Wittenberg et al. 2006; Taschetto et al. 2014; Graham et al. 2017; Planton et al. 2020; Jiang et al. 2021). This is primarily because the enhanced climatological zonal temperature gradient induces a stronger zonal advective feedback in the western equatorial Pacific and favors the westward extension of ENSO SST anomalies (Graham et al. 2017; Jiang et al. 2021). Besides affecting the oceanic feedback, the cold tongue bias could shift the rising branch of Walker circulation westward. As a result, the wind–SST feedback is overestimated in the western equatorial Pacific but underestimated in

Denotes content that is immediately available upon publication as open access.

Supplemental information related to this paper is available at the Journals Online website: https://doi.org/10.1175/JCLI-D-21-0470.s1.

Corresponding author: Xian Wu, xianwu@ucar.edu

DOI: 10.1175/JCLI-D-21-0470.1

the whole equatorial Pacific in some models (Ham and Kug 2011; Bayr et al. 2018). The influence of mean-state bias on ENSO amplitude is complex and masked in many models due to the error compensation of ENSO feedbacks. For example, a model can still simulate realistic ENSO amplitude when underestimating both the positive wind–SST feedback and negative heat flux–SST feedback (Bellenger et al. 2014; Bayr et al. 2019a).

The cold tongue bias can also degrade the models' ability to predict ENSO. Models with a cold tongue bias show errors in predicting the pattern of ENSO; in particular, they show negative correlation skill in their ENSO forecasts of SST anomalies in the western Pacific in both dynamical (Ham et al. 2014) and statistical forecasts (Ding et al. 2018). Forecast errors of ENSO amplitude are also found to be related to the biases of SST and upper-ocean temperature in the equatorial Pacific (Manganello and Huang 2009; Kim et al. 2017). Besides the forecast errors of pattern and amplitude of ENSO events, a recent study by Wu et al. (2021a) notes that the low skill in predicting the termination of El Niño events and the subsequent transition to La Niña is related to the strong cold tongue bias of the retrospective forecasts conducted with Community Earth System Model, version 1 (CESM1). However, the errors regarding the phase transition of El Niño are absent in the "perfect model" prediction experiments performed with the same model (Wu et al. 2021b) because such idealized predictions do not have the issues that arise in the retrospective forecasts summarized below.

Errors in operational dynamical forecasts arise not only from the inherent model biases discussed above, but also from the initialization methods, including uncertainties in reproducing the true initial conditions and incompatibilities between the initial states and the model dynamics. When forecasts are initialized with full-field oceanic states derived from observations, the forecasts will drift toward the model's own climatology as the forecasts progress (Misra et al. 2008; Magnusson et al. 2013). In addition to the gradual model drift, the full-field initialization may lead to a rapid initial adjustment of the model if there is a large imbalance between the prescribed initial conditions and the model dynamics, known as the initialization shock problem (Magnusson et al. 2013).

Understanding the causes of cold tongue bias and related ENSO forecast errors is important from the standpoint of seasonal prediction skill in ENSO-related tropical rainfall and extratropical teleconnections (Bayr et al. 2019b; Ding et al. 2020). In this paper, we analyze the climatological bias of the equatorial Pacific and its impact on ENSO forecasts in a suite of multiyear CESM1 forecasts initialized with full-field oceanic states in March, June, and November during 1954–2015. First, we examine in detail the origins of cold tongue bias in the CESM1 forecasts, including the inherent climatological bias of CESM1, imbalance between the initial conditions and model dynamics, and errors in the ocean initial conditions. Then we investigate the forecast errors in ENSO characteristics and teleconnections, and their relationship with the cold tongue bias of the forecasts and initial condition error.

The rest of this paper is organized as follows. The model, experiments, and analysis are described in section 2. Section 3 presents the analyses of cold tongue bias and ENSO errors in the forecasts and the dynamical processes underlying these errors. Results are summarized and discussed in section 4.

2. Model experiments and analysis methods

a. CESM1

The simulations and forecasts used in this study were run with the CESM1, an earth system model consisting of interactive atmosphere, ocean, land, and ice components (Hurrell et al. 2013). All of model components were run at nominal 1° horizontal resolution, including the Community Atmosphere Model, version 5 (CAM5; Neale et al. 2012) with 30 vertical levels; the Parallel Ocean Program, version 2 (POP2; Smith et al. 2010) with 60 vertical levels; the Community Land Model, version 4 (CLM4; Lawrence et al. 2011); and the Los Alamos National Laboratory Community Ice Code, version 4 (CICE4; Hunke and Lipscomb 2008).

The CESM1 produces one of the most realistic simulations of the ENSO phenomenon among global climate models (Bellenger et al. 2014). It reproduces the broad spectral peak of ENSO in the 3–6-yr band, the asymmetric amplitude and pattern between El Niño and La Niña, and the wide range of durations of ENSO events (DiNezio et al. 2017a; Wu et al. 2019). The CESM1 shows high skill in predicting the duration of El Niño and La Niña up to two years in advance when initialized from particular ocean states (DiNezio et al. 2017a,b; Wu et al. 2021a,b). However, the free-running preindustrial control simulations of CESM1 overestimate the amplitude of ENSO by about 20% and show an excessive extension of ENSO anomalies into the western equatorial Pacific compared to observations (DiNezio et al. 2017a; Capotondi et al. 2020). The initialized forecasts of CESM1 show large biases in predicting ENSO pattern and duration especially when the climatological cold tongue bias is strong in the forecasts initialized in particular seasons (Wu et al. 2021a).

b. CESM1 retrospective forecasts and uninitialized simulations

We analyze three sets of multiyear CESM1 ensemble forecasts initialized on the first day of March, June, and November for each year from 1954 to 2015. The November-initialized forecasts are taken from the CESM Decadal Prediction Large Ensemble (Yeager et al. 2018) and the ensembles initialized in March and June are from Wu et al. (2021a). All forecast ensembles use the same model and component configuration as in the CESM1 Large Ensemble Project (CESM1 LE; Kay et al. 2015). For each year and calendar month, ensemble forecasts are initialized with identical ocean and sea ice conditions for the initialization date, and the ensemble spread is generated by adding small perturbations of an order of 10^{-14} to the atmospheric initial conditions. The ensembles initialized in March, June, and November have 10, 20, and 40 members and are integrated over 30, 27, and 34 months, respectively. The initialization months and forecast length were selected to investigate the predictability of ENSO events with lead times up to 2 years and the seasonal dependence of forecast skill.

A bootstrap analysis of the 40-member November-initialized forecasts showed that an ensemble size of 10 was sufficient to estimate the ensemble mean signal of ENSO predictions, although the ensemble spread is slightly underestimated compared to the 40-member forecasts (Wu et al. 2021a). The ocean and sea ice initial conditions for all ensembles were generated by forcing the ocean (POP2) and sea ice (CICE4) component models with historical atmospheric and surface flux fields. This "forced ocean–sea ice simulation" (FOSI) can reproduce key features of observed ocean and sea ice (e.g., Yeager and Danabasoglu 2014; Yeager et al. 2015), but its deficiency in simulating the equatorial Pacific mean climate and ENSO variability will be examined. The atmosphere and land initial conditions are obtained from the CESM1 LE (Kay et al. 2015) for the November-initialized forecasts and from an atmosphere–land model (CAM5–CLM4) simulation prescribed with monthly ocean and sea ice fields simulated by the FOSI for the March- and June-initialized forecasts. The different techniques for initializing atmosphere and land models are not expected affect the predictions of tropical Pacific SSTs, whose predictability is mostly governed by oceanic memory. All forecasts follow historical (1954–2005) and representative concentration pathway 8.5 (RCP8.5; 2006–15) radiative forcings.

We further compare initialized forecasts with uninitialized CESM1 LE to estimate the mean-state errors that arise from initialization problems. It is noted that the CESM1 LE only has model bias, and the initialized forecasts suffer from both model bias and initialization problems. We make use of the 40-member CESM1 LE during the forecast period 1954–2015. The first member of the CESM1 LE is initialized with oceanic and atmospheric conditions of year 401 of the CESM1 preindustrial control simulation and integrated from 1850 to 2100 under the historical (prior to 2006) and RCP8.5 (2006–2100) forcings. The other 39 members are branched from the first member on 1 January 1920 with small perturbations applied to the atmospheric initial conditions (order of 10^{-14} K).

c. Observational datasets

We compare the forecasts, uninitialized simulations, and ocean initial conditions used for initializing the forecasts against several observational and reanalysis datasets over the period of 1954–2017. Observed SSTs are taken from the Hadley Centre Sea Ice and SST dataset (HadISST; Rayner et al. 2003) at 1° spatial resolution. The near-surface air temperature over land is taken from the Berkeley Earth Surface Temperature (BEST) station-based dataset at 1° spatial resolution (Rohde et al. 2013). We define the thermocline depth as the depth of maximum vertical ocean temperature gradient derived based on the ocean temperature from European Centre for Medium-Range Weather Forecasts (ECMWF) Ocean Reanalysis System 4 (ORAS4; Balmaseda et al. 2013) on 1° horizontal resolution with 42 vertical levels. Several other ocean reanalysis datasets are also used to validate the estimation of observed equatorial Pacific thermocline depth (Fig. S1 in the online supplemental material), including the Simple Ocean Data Assimilation reanalysis, version 2.2.4 (SODA; Carton and Giese 2008), version 4 of the Met Office Hadley Centre EN4 (EN4; Good et al. 2013) with two different sets of bias corrections by Levitus et al. (2009; EN4l09) and Gouretski and Reseghetti (2010; EN4g10), Estimating the Circulation and Climate of the Ocean Version 4, Release 4 (ECCOV4R4; Forget et al. 2015), global ocean data assimilation system (GODAS; Behringer and Xue 2004), and the global objective analyses of ocean data from the International Comprehensive Ocean and Atmosphere Dataset and the Kobe Collection (ICOADS_Kobe; Ishii et al. 2005). The surface wind components, sea level pressure (SLP), precipitation, and 200-hPa geopotential height (Z200) are taken from the National Centers for Environmental Prediction–National Center for Atmospheric Research (NCEP–NCAR) reanalysis (Kalnay et al. 1996) on a 2.5° grid. The shortwave flux, latent heat flux, and net heat flux at surface are taken from the Objectively Analyzed Air–Sea Fluxes (OAFlux; Yu and Weller 2007) on a 1° grid for 1984–2009. We also test the robustness of atmospheric composites results in Fig. 7 using the Japanese 55-year Reanalysis (JRA55; Kobayashi et al. 2015) for surface wind, SLP, ocean precipitation, and Z200, and the Climatic Research Unit time series (CRU; Harris et al. 2014) for land precipitation during 1958–2017 (Fig. S9). We regrid the observational data to the same grid as the model output before calculating their difference.

d. Analysis methods

The drifting climatology of the ensemble forecasts is calculated separately for each initialization month by averaging the ensemble mean forecasts across the initialization years from 1958 to 2015 for each lead time. We define forecast anomalies as deviations from the climatology. The effect of external radiative forcing is removed by subtracting a quadratic trend computed from the ensemble mean anomalies for each lead time following Yeager et al. (2018). We remove a quadratic trend instead of a linear trend because the forecasts after 2000 show a more pronounced warming trend than the earlier period. The observations are treated in a similar manner, with the monthly climatology calculated for 1958–2015, and quadratically detrending applied to the monthly anomalies. The influence of external forcing on the ENSO forecast skill is small for short lead times but becomes significant for lead time longer than one year (not shown). The monthly climatology inherent to the CESM1 is calculated using the 40-member ensemble mean of CESM1 LE for the forecast period of 1958–2015. The effect of radiative forcing is removed by subtracting the monthly ensemble mean anomalies from individual ensemble members.

The temporal evolution of ENSO events is tracked using the Niño-3.4 index defined as SST anomalies averaged over the Niño-3.4 region (5°S–5°N, 170°–120°W). Following Wu et al. (2019, 2021a), observed ENSO events are defined when the absolute value of the detrended Niño-3.4 (|Niño-3.4|) index smoothed with a 3-month running mean filter is greater than 0.75 standard deviations in any month from October to February. The standard deviation is computed separately for each month during October to February over the period 1954–2017. We denote the year of initial ENSO development

as year 0 and the months of the year as Jan^0, Feb^0, …, and Dec^0. We composite ensemble forecasts initialized in Nov^{-1}, Mar^0, Jun^0, Nov^0, Mar^{+1}, and Jun^{+1} of observed ENSO events. ENSO events are further classified into 1-yr events when the smoothed |Niño-3.4| index drops below 0.5 standard deviations in any month from Oct^{+1} to Feb^{+2}, and otherwise into 2-yr events. During 1954–2017, we identify ten 1-yr El Niño (1963, 1965, 1972, 1982, 1991, 1994, 1997, 2002, 2006, and 2009), five 2-yr El Niño (1957, 1968, 1976, 1986, and 2014), four 1-yr La Niña (1964, 1988, 1995, and 2005), and eight 2-yr La Niña events (1954, 1970, 1973, 1983, 1998, 2007, 2010, and 2016), with the list of years indicating year 0. Two-year ENSO events are selected based on the Niño-3.4 index in two consecutive winter seasons, which does not guarantee the continuity during the summer between the two winters. We define the onset and termination of ENSO events in the forecasts when the |Niño-3.4| first exceeds and drops below 0.5°C, respectively. Readers are referred to Wu et al. (2021a) for further details of the analysis methods. The ENSO variability in the CESM1 LE is evaluated based on the ENSO events identified using the same method as for observations applied to all 40 members during 1954–2015. We compare the climatology and composite ENSO events in the initialized CESM1 forecasts with those in observations and the CESM1 LE. The statistical significance of the composite anomalies is assessed using a two-tailed Student's t test at the confidence level of 95%.

3. Results

a. Climatological errors in the equatorial Pacific

The climatological seasonal cycle of SST, surface wind, and thermocline depth in the equatorial Pacific for the forecasts initialized in November, March, and June are compared with observations and CESM1 LE (Fig. 1). The three sets of forecasts capture the seasonal intensification of the SST cold tongue during boreal summer and autumn (Figs. 1a–d). In both the forecasts and observations (Figs. 1a–d), the SST cooling intensifies in the eastern equatorial Pacific when the equatorial southerly winds start to develop in late boreal spring to early summer (May–June) in association with the seasonal northward migration of the ITCZ (Mitchell and Wallace 1992; Xie 1994). During summer and early autumn (June–September), the eastern equatorial Pacific SST cooling and southeasterly winds extend to the central-western equatorial Pacific. The intensification and westward extension of the Pacific cold tongue and associated climatological easterly winds are overestimated in the forecasts (Fig. 1e). Climatological SSTs in the forecasts show a cooling bias of up to −4.3°C around Sep^0 in the first year of the March-initialized forecasts, together with an excessive westward shift of the Pacific warm pool edge (28°C) by up to 35° of longitude during Sep^0–Mar^{+1} of the March- and June-initialized forecasts relative to observations (Fig. 1e). The SST cooling and easterly wind biases over the western-central equatorial Pacific linger into early boreal spring in the forecasts, resulting in a 2-month delay of the warmest season in the equatorial eastern Pacific (February–April in observations and April–June in all forecast ensembles). These climatological SST and wind biases are partly inherent to the model's climatology (Fig. 1f), since the deviations of forecasts from the CESM1 LE (Fig. 1g) are smaller than that from the observations (Fig. 1e). The biases in all three sets of forecasts are statistically significant at the 99.5% confidence level despite the different ensemble sizes, according to the bootstrap method across the ensemble members (Fig. S2, top).

The development of the SST cooling bias in the eastern equatorial Pacific is preceded by a negative (shallow) thermocline depth bias that propagates eastward from the western-central equatorial Pacific after the initialization (Fig. 1e). The initial "shallow" thermocline bias is rooted in errors in the initial condition data from FOSI, which simulates shallower climatological thermocline in the western-central Pacific compared to the ORAS4 (Fig. 2) and other six ocean reanalysis datasets (Fig. S1a). The equatorial Pacific SST simulated by the FOSI is overall warmer than the observations, suggesting that the quick development of cold tongue SST bias in the March- and June-initialized forecasts is not an amplification of the initial SST errors. The causes of FOSI errors in simulating the observed thermocline depth and SST in the equatorial Pacific require further examination. It could be partly caused by the CESM1's inherent bias in simulating the depth and slope of the thermocline in the equatorial Pacific (Fig. 1f), the errors in surface winds in the equatorial and off-equatorial Pacific used to force the FOSI [not shown; see Yeager et al. (2018) for more details about the wind datasets used in FOSI], or/and the deficiencies in simulating other processes that influence climatological SSTs.

The cold tongue SST bias in year 0 is larger in the March- and June-initialized forecasts compared to the November-initialized forecasts (Fig. 1e), and this difference among the three forecast sets is well beyond the range of uncertainty due to sampling of ensemble members (Fig. S2, bottom). The dependence of cold tongue bias on the initialization month of the forecasts is associated with the strong seasonality of thermocline–SST feedback in the equatorial eastern Pacific (Fig. 3a). In observations, CESM1 LE, and forecasts, the strength of the feedback, measured by the regression coefficient of SST on the thermocline depth in the eastern equatorial Pacific (Niño-3 region), is smallest during boreal spring (March–May; $-0.02°C\ m^{-1}$ in CESM1 LE) and largest in late summer–autumn (August–November; $0.11°C\ m^{-1}$ in CESM1 LE). The seasonality of the SST sensitivity to thermocline depth is associated with the seasonal change in climatological upwelling in the eastern equatorial Pacific (not shown). In the March- and June-initialized forecasts, the initial thermocline shoaling bias in the western-central equatorial Pacific propagates into the eastern basin during boreal summer–autumn, inducing large negative SST bias (Fig. 1e). In the November-initialized forecasts, by contrast, the thermocline shoaling bias arriving in boreal spring produces a smaller SST bias in the eastern equatorial Pacific. Note that the correlation between the thermocline and SST mainly represents interannual variability, as the seasonal cycle of cold tongue involves little change in the thermocline depth (Chang and Philander 1994;

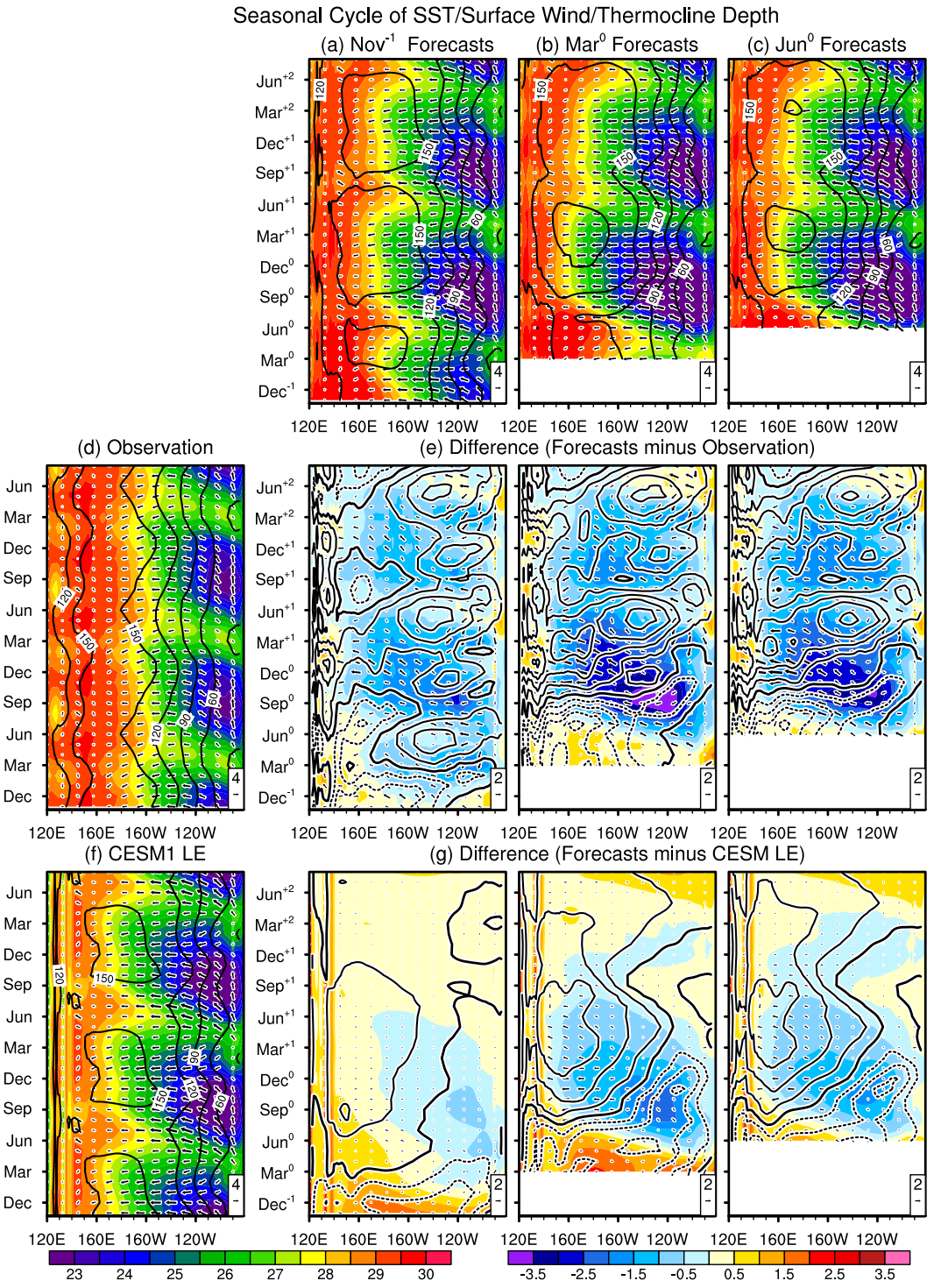

FIG. 1. Longitude–time sections of climatological monthly SST (°C; shading), thermocline depth (contours at intervals of 30 m), and surface wind (m s^{-1}; vectors) in the equatorial Pacific (3°S–3°N) for the ensemble forecasts initialized in (a) November, (b) March, and (c) June (superscripts on the months along the *y* axis indicate the first year when all forecasts overlap), (d) observations (HadISST, ORAS4, and NCEP–NCAR) and (f) CESM1 LE during 1958–2015. Note that the climatologies of the forecasts are a function of lead time, whereas those of the observations and CESM1 LE are simply repeated for clarity. The deviations of the forecast climatologies from (e) observations and (g) CESM1 LE for SST (°C; shading), thermocline depth (contours at intervals of 10 m; zero contours thickened and negative contours dotted), and surface wind (m s^{-1}; vectors). The thermocline depth is smoothed with a nine-point running-mean filter in the longitudinal direction. The statistical significance of Fig. 1e is shown in Fig. S2.

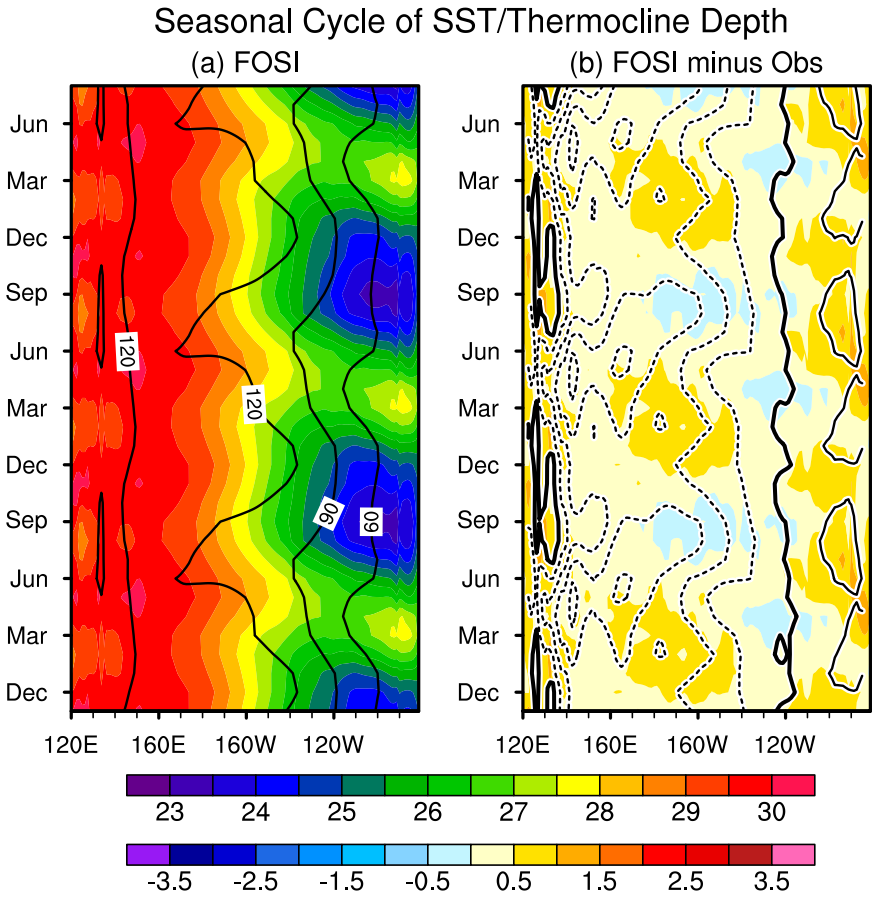

FIG. 2. (a) Longitude–time sections of climatological SST (°C; shading) and thermocline depth (contours at intervals of 30 m) in the equatorial Pacific (3°S–3°N) during 1958–2015 for the FOSI. (b) The difference of climatological SST (°C; shading) and thermocline depth (contours at intervals of 10 m; zero contours thickened and negative contours dotted) between the FOSI and observations (HadISST and ORAS4). The thermocline depth is smoothed with a nine-point running-mean filter in the longitudinal direction.

Xie 1994). However, the thermocline–SST feedback that operates in interannual variability appears to be important for amplifying the influence of initial climatological thermocline shoaling bias on climatological SST bias. Our results are consistent with a recent study by Siongco et al. (2020), which also shows that the cold tongue bias of CESM1 hindcasts develops faster during boreal summer–autumn than other seasons due to the strengthening of vertical temperature advection in the eastern equatorial Pacific.

The three sets of forecasts, especially those initialized in March and June, display a pronounced cooling bias in the first year (year 0) relative to subsequent years of the forecast (Fig. 1e). This strong initial cooling bias is associated with the imbalance of the initial ocean state and the model's dynamics as shown in the difference between forecasts and CESM1 LE (Fig. 1g). The initial thermocline shoaling anomalies across the equatorial Pacific leads to an SST cooling response in year 0 of the forecasts relative to CESM1 LE. As a result, the climatology of forecasts shows pronounced deviations from the model's climatology in year 0 before stabilizing. The difference in climatological surface winds between forecasts and CESM1 LE is consistently very small throughout the 2-yr forecasts, suggesting that the initial model adjustment is mostly driven by oceanic processes.

b. *Forecast errors of ENSO characteristics*

Forecast errors of the temporal evolution and amplitude of ENSO events, and the dependency of error development on the initialization season, are assessed based on the predictions of Niño-3.4 SST index. Figures 4a and 4b show the time series of the Niño-3.4 index composited for all El Niño and La Niña events during 1954–2015 in observations and ensemble-mean forecasts initialized at different lead times. The onset of El Niño and La Niña (defined using a threshold of $|\text{Niño-3.4}| > 0.5°\text{C}$) in the summer of year 0 is not captured in the forecasts initialized in Nov^{-1}, which is probably related to the overall low predictability of the onset of ENSO events before boreal spring (e.g., Torrence and Webster 1998; Tippett and L'Heureux 2020) rather than the model errors. One exception from this composite result is the onset of La Niña

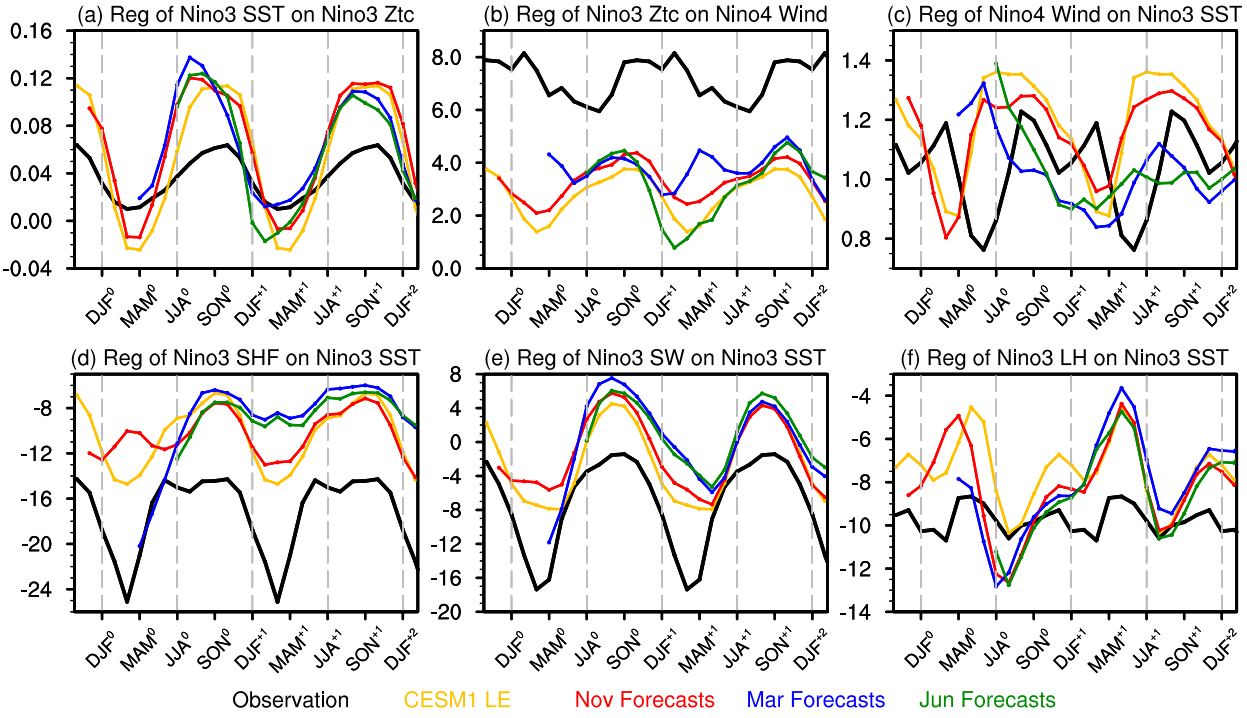

FIG. 3. Seasonal mean regression coefficients between different variables in the observations (black curves; HadISST, ORAS4, NCEP–NCAR, and OAFlux), CESM1 LE (yellow curves), November- (red curves), March- (blue curves), and June-initialized (green curves) forecasts during 1954–2015 (1984–2009 for observed surface fluxes). (a) Regression of SST on thermocline depth (°C m^{-1}), (b) regression of thermocline depth on surface wind (s), (c) regression of surface wind on SST (m s^{-1} °C^{-1}), (d) regression of net surface heat flux on SST (W m^{-2} °C^{-1}), (e) regression of surface shortwave flux on SST (W m^{-2} °C^{-1}), and (f) regression of surface latent heat flux on SST (W m^{-2} °C^{-1}). The surface winds are averaged over the Niño-4 region (5°S–5°N, 160°E–150°W), and all other variables are averaged over the Niño-3 region (5°S–5°N, 150°–90°W). Note that the regression coefficients in the forecasts are a function of lead time, whereas those of the observations and CESM1 LE are simply repeated for clarity.

events following strong El Niño, which can be predicted in the forecasts initialized from the preceding El Niño peak (not shown). The onset of El Niño and La Niña is first seen in the Mar^0-initialized forecasts, although the Niño-3.4 SST anomalies quickly dissipate in the following autumn. The Jun^0-initialized forecasts show improvement, but the predicted peak of El Niño and La Niña is weaker and occurs too early compared to observations. The shift in the timing of peak is associated with the extensive westward shift of maximum ENSO SST anomalies in the forecasts (cf. Fig. 5).

After the peak, all forecasts of El Niño show a warm SST bias in year +1 of about 0.6°C, while all forecasts of La Niña capture the returning of La Niña as seen in observations (Figs. 4a,b). To assess the forecast errors of ENSO event duration, we classify El Niño and La Niña events into those lasting one year (Figs. 4c,d) and two years (Figs. 4e,f). The forecasts initialized in and after Jun^0 successfully capture the termination of 1-yr El Niño and 1-yr La Niña events (defined using a threshold of |Niño-3.4| < 0.5°C), but do not capture the transition to the opposite ENSO state in year +1 (Figs. 4c,d). On the other hand, the forecasts show good performance in predicting the continuation of 2-yr ENSO events. The reintensification of 2-yr El Niño events is captured in the forecasts initialized in/after Nov^0, and the persistence of 2-yr La Niña events is predicted in all six sets of forecasts (Figs. 4e,f). The mechanisms driving the long-term predictability of 1-yr and 2-yr ENSO events have been explored by Wu et al. (2021a) and DiNezio et al. (2017b). Because 1-yr El Niño accounts for a large portion of El Niño events (10 out of 15) and 2-yr La Niña dominates the signal of all La Niña events (8 out of 12), the model shows better performance in predicting the overall duration of La Niña than El Niño events. In the remainder of this section, we show the results of our dynamical analysis for 1-yr El Niño events and discuss the similarities and differences with the other types of ENSO events whose results are shown in the supplemental materials.

To illustrate the dynamical processes underpinning the forecast errors in Niño-3.4 SST index, the spatiotemporal evolutions of SST, surface wind, and thermocline depth anomalies in the forecasts of 1-yr El Niño are compared with observations (Fig. 5; see Fig. S3 for the results of other types of ENSO events and Fig. S4 for the statistical significance of the composites). In the Mar^0- and Jun^0-initialized forecasts (Figs. 5b,c), the SST warming and surface westerly wind anomalies associated with 1-yr El Niño quickly extend toward the far western Pacific during boreal summer (Jun^0–Aug^0), when the mean-state cold tongue bias intensifies (Fig. 1e) and causes biased oceanic and atmospheric feedbacks in the

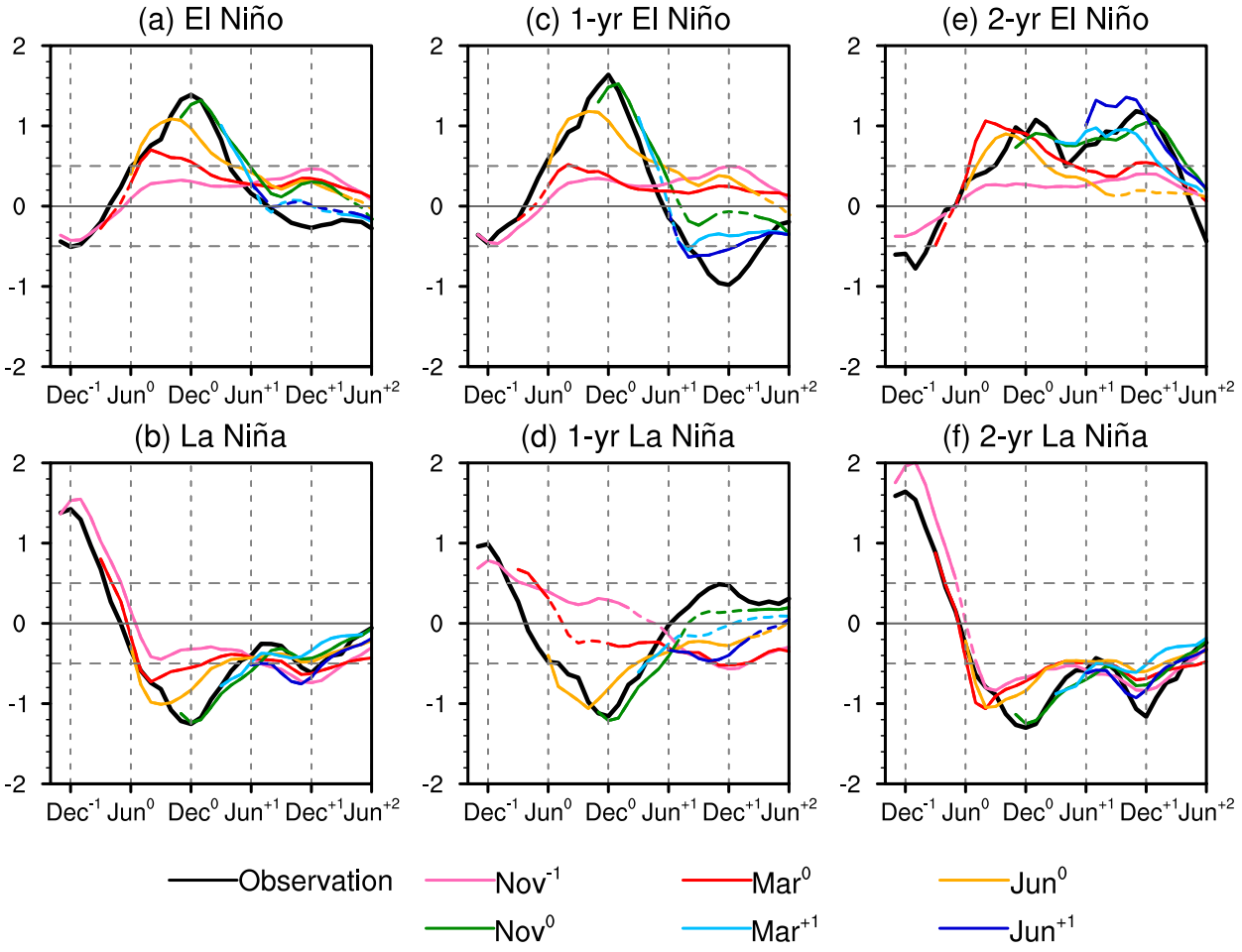

FIG. 4. Time series of the Niño-3.4 index (°C) composited for (a) all El Niño, (b) all La Niña, (c) 1-yr El Niño, (d) 1-yr La Niña, (e) 2-yr El Niño, and (f) 2-yr La Niña events in the observations (HadISST; black curves) and ensemble-mean forecasts (colored curves) during 1954–2015. The forecasts are initialized in Nov^{-1} (pink), Mar^{0} (red), Jun^{0} (yellow), Nov^{0} (green), Mar^{+1} (light blue), and Jun^{+1} (dark blue). The dashed horizonal lines denote the ±0.5°C threshold. The solid portions of the colored curves indicate that the composite forecasts are significantly different from zero at the 95% confidence level.

equatorial Pacific (Fig. 3). The difference between the forecasts and observations during Jun^{0}–Apr^{+1} displays a zonal dipole pattern in the equatorial Pacific, indicating a westward shift of the SST and wind anomalies (Fig. 5e). In the Mar^{0}- and Jun^{0}-initialized forecasts, the weaker SST warming over the central-eastern equatorial Pacific (180°–80°W) during the El Niño development phase is related to the underestimated wind–SST feedback during SON^{0}–DJF^{+1} (Fig. 3c) and weaker positive thermocline depth anomalies in the eastern equatorial Pacific compared to the observations (Fig. 5e). The weakened thermocline deepening is linked to the simultaneous weakened westerly wind anomalies over the western-central Pacific (160°E–180°) and the underestimated wind–thermocline feedback in the eastern equatorial Pacific in forecasts (Fig. 3b). Furthermore, the errors in the initial thermocline depth anomalies also contribute to weaker El Niño amplitude, which show weaker thermocline deepening in the central-eastern equatorial Pacific at the initialization in the Mar^{0}- and Jun^{0}-initialized forecasts than observations.

Besides the pattern and amplitude biases of 1-yr El Niño forecasts during Jun^{0}–Apr^{+1}, the biased SST warming and westerly wind anomalies over the western equatorial Pacific persist after the mature phase. In association with the lingering westerly anomalies and weaker peak amplitude of 1-yr El Niño, the thermocline shoaling over the western equatorial Pacific is too weak and does not propagate into the eastern equatorial Pacific after the mature phase in the Mar^{0}- and Jun^{0}-initialized forecasts, resulting in the failure of predicting the La Niña state in year +1. The lingering ENSO SST and wind anomalies in the western Pacific is likely driven by the overestimated wind–SST feedback during AMJ^{+1}–JAS^{+1} in the forecasts (Fig. 3c). In addition, the damping effect of net surface heat flux on SST in the eastern equatorial Pacific is underestimated in the Mar^{0}- and Jun^{0}-initialized forecasts (Fig. 3d), which could contribute to the lingering ENSO duration. The underestimation of the heat flux–SST feedback is largely contributed by the shortwave–SST feedback (Fig. 3e) and partly by the latent heat–SST feedback during

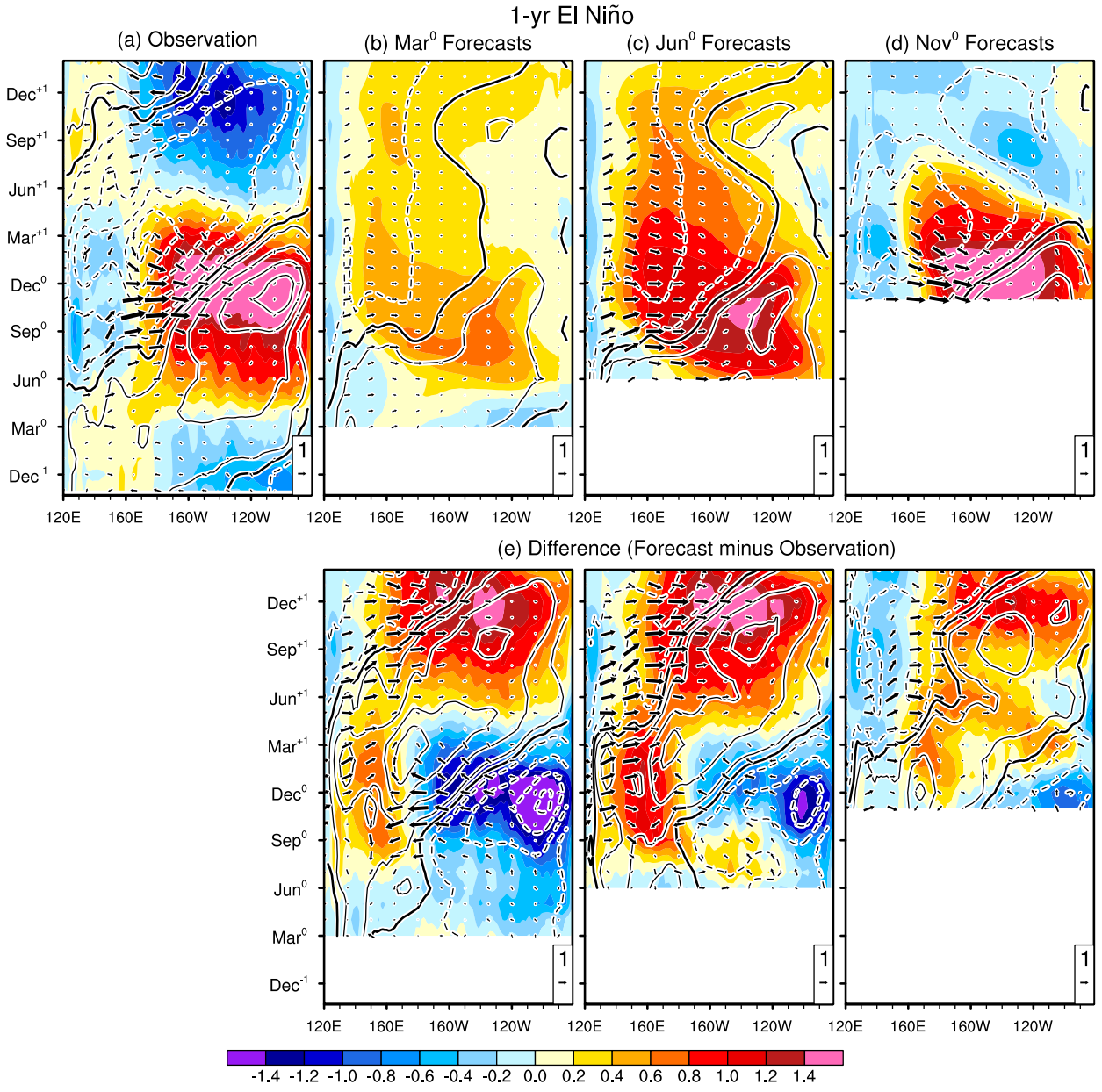

FIG. 5. Longitude–time sections of SST (°C; shading), thermocline depth (contours at intervals of 8 m starting at ±4 m; zero contours thickened and negative contours dashed), and surface wind (m s^{-1}; vectors) anomalies in the equatorial Pacific (3°S–3°N) composited for 1-yr El Niño in the (a) observations (HadISST, ORAS4, and NCEP–NCAR), ensemble-mean forecasts initialized in (b) Mar^0, (c) Jun^0, (d) Nov^0, and (e) the difference between the forecasts and observations. The thermocline depth anomalies are smoothed with a nine-point running-mean filter in the longitudinal direction and a 1–2–1 filter in the time direction in both observations and forecasts. The composites for other types of ENSO events are shown in Fig. S3, and the statistical significance of these composite anomalies is shown in Fig. S4.

SON^0–JJA^{+1}(Fig. 3f). Previous studies also find that the shortwave–SST feedback is important to the simulation of ENSO phase locking (Wengel et al. 2018; Bayr et al. 2021).

In contrast, the biases of spatial pattern, peak amplitude, and phase transition of 1-yr El Niño events are reduced in the Nov^0-initialized forecasts (Figs. 5d,e and Fig. S4), for which the mean-state cold tongue bias is weaker and the initialization is closer to the El Niño peak than the Mar^0- and Jun^0-initialized forecasts (Fig. 1e). In particular, the phase transition from El Niño to La Niña is captured in the Nov^0-initialized forecasts, although the amplitude of subsequent La Niña is underestimated presumably due to the smaller initial thermocline depth anomalies in FOSI. The forecasts of the other three types of ENSO events also show westward-shifted pattern bias and weaker amplitude of anomalies over the central-eastern Pacific, and these biases are stronger in the Mar^0- and Jun^0-initialized

forecasts than the Nov^0-initialized forecasts (Fig. S3). Similar to 1-yr El Niño, the Mar^0 and Jun^0-initialized forecasts fail to capture the phase transition of 1-yr La Niña but show biased weak equatorial Pacific cooling throughout year +1. In contrast, the continuation of 2-yr El Niño is predicted by the Nov^0-initialized forecasts, and the continuation of 2-yr La Niña events is predicted in all three sets of forecasts, despite the pattern and amplitude biases in year +1.

To understand why the surface wind anomalies over the far western equatorial Pacific tend to linger into the second year and prolong equatorial Pacific warming in the 1-yr El Niño forecasts, we examine SST anomalies in the key ocean basins that could influence these wind anomalies. Figure 6 compares the longitude–time sections and time series of SST and surface wind anomalies over the equatorial Pacific, the tropical Indian Ocean (10°S–0°), and the tropical North Atlantic (0°–20°N) composited for 1-yr El Niño events in the observations, forecasts initialized in Jun^0 and Nov^0, and CESM1 LE (see Fig. S5 for the results of other types of ENSO events and Fig. S6 for the statistical significance of the composites). In observations, the tropical Indian and Atlantic Oceans warm up during the mature phase (Dec^0–Feb^{+1}) of 1-yr El Niño due to tropical atmospheric adjustments to the equatorial Pacific SST warming (Fig. 6a; Xie and Carton 2004; Schott et al. 2009). The Jun^0-initialized forecasts, however, underestimate the warming of tropical Indian and Atlantic Oceans during Dec^0–Feb^{+1} presumably due to the weaker El Niño warming over the eastern equatorial Pacific (Figs. 6b,e,h; the Mar^0 forecasts show similar results). The underestimated Indian and Atlantic Ocean warming and overestimated warming over the western equatorial Pacific could work together to modulate the interbasin SST contrast and contribute to the biased persistence of surface westerly wind anomalies in the spring after the El Niño peak in the Jun^0-initialized forecasts. Figure 6h more quantitively show that the cooling bias of the Indian and Atlantic Oceans contributes to about 40% of the bias in the positive interbasin SST contrast during Dec^0–Feb^{+1}, while the SST warming bias over the western Pacific is the dominant factor. The Nov^0-initialized forecasts show similar SST and wind biases during Dec^0–Feb^{+1} as in the Jun^0-initialized forecasts, indicating these biases are inherent to the model, but they are much reduced in the Nov^0-initialized forecasts due to short lead times (Figs. 6f,i).

We note that the westward shift of ENSO anomaly pattern and SST warming bias over the western equatorial Pacific is a bias inherent to the CESM1 (Figs. 6d,g,j). Nonetheless, this model reproduces the observed frequency of 1-yr El Niño events in the control simulation (Wu et al. 2019). In CESM1 LE, the delayed warming of the tropical Indian and Atlantic Oceans after the peak of 1-yr El Niño is much stronger than observations (Figs. 6d,g,j). The warming bias of the Indian and Atlantic Oceans balances with the SST warming bias over the western-central equatorial Pacific, resulting in a smaller bias in the interbasin SST contrast and wind anomalies during the boreal spring after the El Niño peak than that in the forecasts. This SST error compensation between the Pacific and other two tropical oceans appears to be important to the smaller wind biases in CESM1 LE. The tropical interbasin interactions on El Niño termination has also been investigated in many previous studies [see Cai et al. (2019) for a review and references therein], but the causality and relative contributions of tropical ocean basins in affecting the surface wind anomalies and ENSO are needed to be examined in the forecast setting.

c. *Forecast errors of ENSO teleconnections*

The forecast errors of tropical SST and precipitation anomalies during the peak of 1-yr El Niño also affect the wintertime atmospheric teleconnections in the Northern Hemisphere. Figure 7 compares SST, surface air temperature over land, surface wind, SLP, precipitation, and Z200 anomalies over the tropics and Northern Hemisphere during Dec^0–Feb^{+1} composited for the 1-yr El Niño events in observations and the Jun^0- and Nov^0-initialized forecasts (see Fig. S7 for the results of other types of ENSO events and Fig. S8 for the statistical significance of the composites). The atmospheric composites in Fig. 7 are robust to the choice observational datasets (Fig. S9). In association with the tropical Pacific SST warming, SLP decreases over the North Pacific, deepening the Aleutian low in both observations and forecasts (Figs. 7a–c, left). In the Jun^0-initialized forecasts, the center of the circulation anomalies exhibits a westward shift of about 10° of longitude and a more zonally elongated pattern compared to observations (Figs. 7a,b, left).

The surface atmospheric biases are mirrored in the upper-tropospheric circulation anomalies (Figs. 7a,b, right). In observations, the increased precipitation and resultant diabatic heating induce a pair of anticyclones at 200 hPa straddling the central equatorial Pacific and a Rossby wave train propagating into the Northern Hemisphere. In the Jun^0-initialized forecasts, the response of extratropical Z200 anomalies is shifted westward and is more zonally elongated compared to observations. The pattern difference between the Jun^0-initialized forecasts and observations displays a slightly tilted zonal dipole pattern in both SLP and Z200 over the midlatitude North Pacific (Fig. 7d). This Z200 anomaly dipole is part of a Rossby wave train originating in southeastern China, which is forced by the biased positive precipitation anomalies over the far western tropical Pacific. In contrast, the biases of extratropical atmospheric circulations are much reduced in the Nov^0-initialized forecasts, consistent with the weaker biases in the pattern and amplitude of tropical SST and precipitation anomalies due to shorter lead times (Fig. 7e). Related to the improved predictions of atmospheric circulation anomalies over the North Pacific, the forecast errors of land surface air temperature anomalies over North America are much weaker in the Nov^0-initialized forecasts than the Jun^0-initialized forecasts (Figs. 7d,e). This result is consistent with the findings by Bayr et al. (2019b), who show that those CMIP5 models with a stronger cold tongue bias tend to simulate a westward shift of atmospheric convection in the tropical Pacific and associated atmospheric teleconnections to the North Pacific during ENSO events.

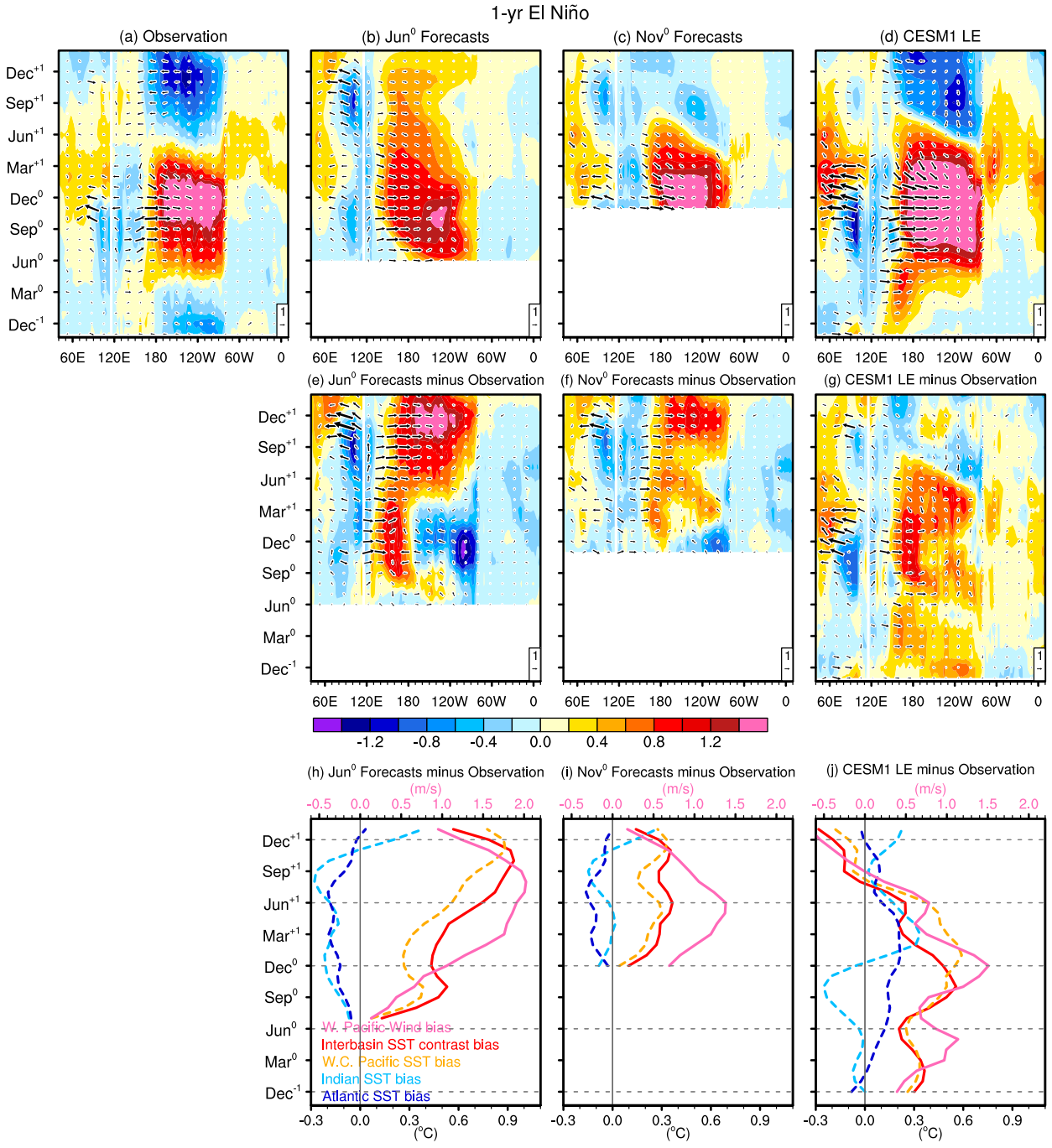

FIG. 6. Longitude–time sections of SST (°C; shading) and surface wind (m s^{-1}; vectors) anomalies in the equatorial Pacific (3°S–3°N), the Indian Ocean (10°S–0°), and the Atlantic (0°–20°N) composited for 1-yr El Niño in the (a) observations (HadISST and NCEP–NCAR), (b) Jun^0 forecasts, (c) Nov^0 forecasts, (d) CESM1 LE, and the deviations of (e) Jun^0 forecasts, (f) Nov^0 forecasts and (g) CESM1 LE relative to the observations. The composites for other types of ENSO events are shown in Fig. S5, and the statistical significance of these composite anomalies is shown in Fig. S6. (h)–(j) Time series of the ocean–atmosphere biases shown in (e) and (f) averaged in different ocean basins: surface wind (m s^{-1}) over the western Pacific (130°–170°E; pink curves), SST (°C) in the western-central Pacific (130°E–140°W; orange curves), the Indian Ocean (40°–120°E; light blue curves), and the Atlantic (80°W–0°; dark blue curves), and the interbasin SST contrast (°C) between the western-central Pacific and Indian/Atlantic Oceans (red curves). The time series are smoothed with a 3-month running filter.

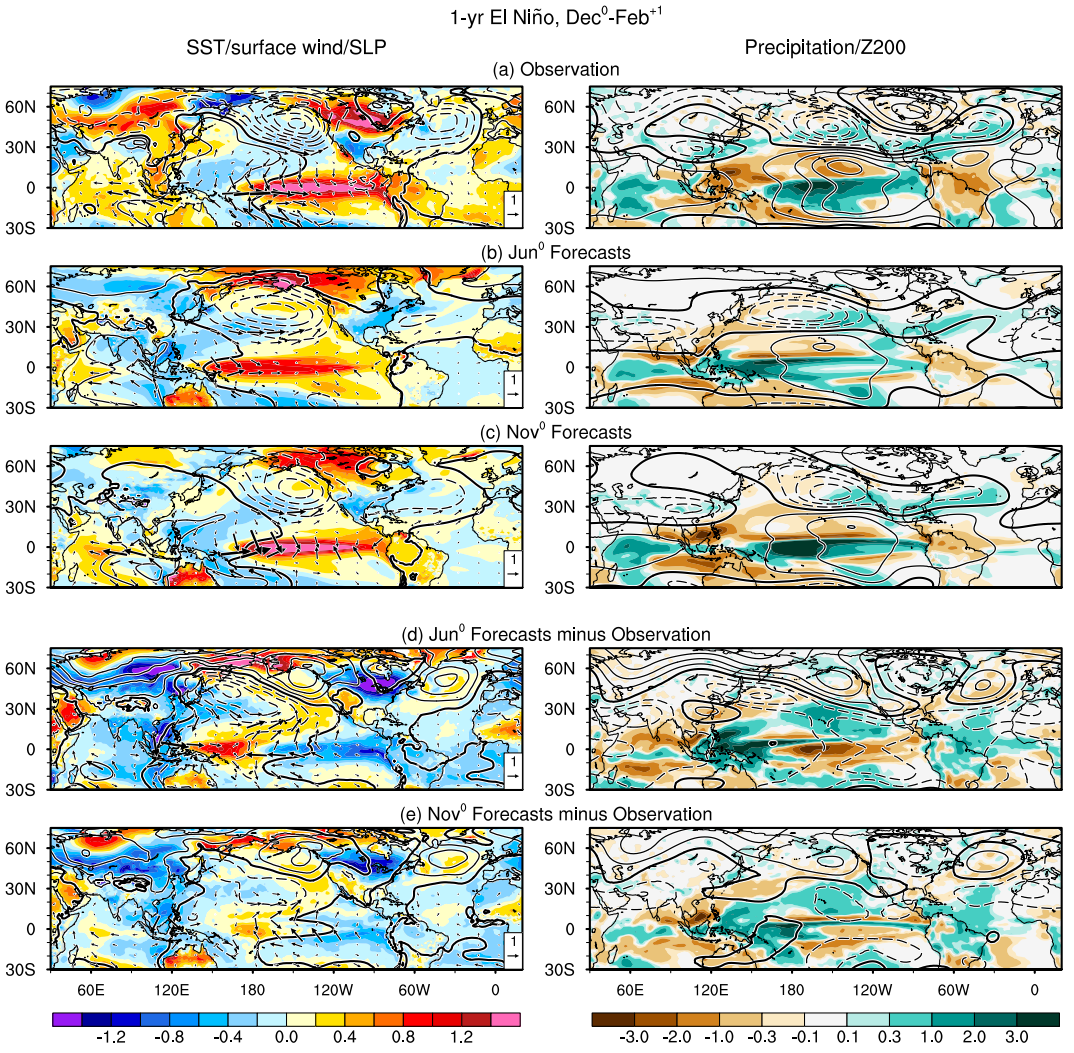

FIG. 7. Maps of (left) SST, land surface air temperature (°C; shading), surface wind (m s^{-1}, vectors) only for tropics and subtropics (30°S–35°N), SLP (contours at intervals of 0.8 hPa; zero contours thickened and negative contours dashed in gray), (right) precipitation (mm day^{-1}; shading), and Z200 (contours at intervals of 15 m; zero contours thickened and negative contours dashed) anomalies composited for 1-yr El Niño events in the (a) observations (HadISST, BEST, ORAS4, and NCEP–NCAR), (b) Jun^0 forecasts, (c) Nov^0 forecasts, and deviations of the (d) Jun^0 forecasts and (e) Nov^0 forecasts from the observations. The composites for other types of ENSO events are shown in Fig. S7, and the statistical significance of these composite anomalies is shown in Fig. S8.

Besides the biases of atmospheric responses over the extratropical North Pacific, we also observe that the anticyclonic SLP anomalies over the western North Pacific (WNP) are much weaker in the Jun^0-initialized forecasts than observations. In observations, anticyclonic SLP anomalies develop over the WNP mainly as a Rossby wave response to the SST cooling and decreased precipitation anomalies over the far western Pacific during El Niño (Fig. 7a; e.g., Wang et al. 2000). The precipitation over the western Pacific could be suppressed not only by local SST cooling but also by the Indian Ocean warming (e.g., Watanabe and Jin 2002). The Jun^0-initialized forecasts predict biased positive SST and precipitation anomalies over the far western equatorial Pacific as well as weaker Indian Ocean warming, resulting in a very weak response of SLP anomalies over the WNP (Fig. 7b). In observations, the surface southerly wind anomalies on the western flank of the anticyclonic SLP anomalies increase the precipitation over East Asia by bringing high moisture content from tropical oceans (Fig. 7a; e.g., Wu et al. 2003). Instead, the Jun^0-initialized forecasts fail to capture these southerly wind anomalies and associated increased precipitation anomalies over East Asia (Figs. 7b,d). The predictions of atmospheric circulation and rainfall anomalies over East Asia are both improved in the Nov^0-initialized forecasts when the ENSO-related tropical SST and precipitation anomalies are more realistically reproduced (Figs. 7c,e).

These forecast errors of atmospheric teleconnections may, in turn, affect surface wind variability over the western equatorial Pacific and the evolution of ENSO states in the second year. In the difference map between the Jun^0 forecasts and observations, the biased SST warming and the southwesterly wind anomalies over the subtropical Pacific resembles the North Pacific meridional mode (NPMM) and potentially contributes to the persistence of equatorial Pacific warming in year +1 (Fig. 7d; e.g., Vimont et al. 2003; Chang et al. 2007; Fang and Yu 2020; Kim and Yu 2021). The weak development of the WNP anomalous anticyclone may also contribute to the ENSO forecast errors in year +1 because the easterly wind anomalies on the southern flank of this anticyclone were suggested as an important factor for El Niño termination (Weisberg and Wang 1997).

Excessively weak tropical interbasin SST adjustments, along with biases in the pattern and amplitude of Northern Hemisphere teleconnections, are found for the forecasts of the other three types of ENSO events (Figs. S5 and S7), although the results for 1-yr La Niña and 2-yr El Niño in observations are largely insignificant at the 95% confidence level due to the small number of events in the composites (Figs. S6 and S8). In contrast to degrading the forecasts of 1-yr ENSO events in year +1, the teleconnection errors over remote oceans during the mature phase of ENSO favor the persistence of 2-yr ENSO events. For example, in the Jun^0-initialized forecasts of 2-yr La Niña (Figs. S5 and S7), the too weak interbasin adjustment, biased negative NPMM, and weak WNP cyclonic SLP circulation may promote the persistence of easterly wind anomalies and SST cooling over the western equatorial Pacific in the second year.

4. Summary and discussions

This study investigates mean-state biases in the equatorial Pacific and their impact on ENSO forecasts based on the retrospective forecasts performed with the CESM1. Three sets of forecasts are initialized in March, June, and November, respectively, to assess the seasonal dependency of the forecast errors. All forecasts regardless of their initialization seasons show a strong cooling bias of the climatological SSTs in the eastern Pacific cold tongue, along with a westward shift of the edge of the Pacific warm pool and excessive climatological easterly winds over the western-central Pacific. This cold tongue bias is amplified in the first year of the forecasts before the model stabilizes at its own climatology at longer lead times. This initial large forecast bias occurs because the initial conditions exhibit a shallower climatological thermocline depth in the western-central equatorial Pacific than the model's climatology. This initial imbalance induces subsequent SST cooling in the first year. The magnitude of this initial amplification of the cold tongue bias depends on the initialization season. The cold tongue bias becomes larger in the March- and June-initialized forecasts relative to the November-initialized forecasts, because the initial thermocline depth errors propagate into the eastern equatorial Pacific when the SST–thermocline feedback is strongest seasonally and thus amplifies the model biases.

Larger ENSO forecast errors are found in the March- and June-initialized forecasts than in the November-initialized forecasts. In the March- and June-initialized forecasts, SST and wind anomalies associated with ENSO migrate excessively westward in the summer season when the cold tongue bias corrupt the simulation of dynamic and thermodynamic feedbacks in the equatorial Pacific. These errors result in weakened SST anomalies over the central-eastern Pacific and hence weaker and earlier peak of ENSO events (as captured by the Niño-3.4 SST index). These forecast errors of ENSO amplitude and peak timing appear to arise from the initialization errors, since the CESM1 LE shows stronger ENSO amplitude and comparable peak timing compared to observations. The underestimation of ENSO amplitude in the forecasts is also associated with weaker initial thermocline anomalies simulated by the FOSI compared to the ocean reanalysis data.

The errors in the pattern and amplitude of ENSO events further affect the prediction of their termination. In particular, the excessively weak amplitude of El Niño events in the forecasts results in a weaker negative thermocline feedback in the equatorial Pacific together with weaker SST warming over the tropical Indian and Atlantic Oceans—regions that are known to influence the termination of ENSO events via atmospheric teleconnections (Cai et al. 2019). The weaker negative feedback from these ocean basins and the too strong ENSO SST anomalies in the western equatorial Pacific lead to biased persistent wind anomalies over the western equatorial Pacific. These biased oceanic and atmospheric processes may work together to cause the excessive tendency of ENSO events to last two years in the forecasts. The erroneous processes associated with the cold tongue bias tend to prolong the duration of ENSO, degrading the predictions of ENSO termination but contributing to the high forecast skill of ENSO continuation for the wrong reason. This may explain why predictions of 2-yr El Niño and 2-yr La Niña events are often better at longer lead times (Figs. 4e,f), although it remains uncertain if the differences among the forecasts are significant considering a small sample size of 2-yr ENSO events.

The ENSO forecast errors further influence the predictions of atmospheric teleconnections, land surface air temperature, and rainfall in the Northern Hemisphere during the mature phase of ENSO. Related to the westward displacement of ENSO SST and precipitation anomalies over the tropical Pacific, the tropospheric and surface atmospheric circulation anomalies over the North Pacific show a westward shift and become more zonally elongated in forecasts compared to observations, leading to the forecast errors of land surface air temperature over North America. Additionally, the pattern bias of ENSO anomalies leads to SLP errors over the western Pacific and to precipitation errors over East Asia. Further studies are needed to examine the forecast errors of ENSO teleconnections in other seasons. These extratropical atmospheric errors during the mature phase of ENSO events may, in turn, affect the predictions of ENSO duration in the following year via the NPMM and WNP anomalous anticyclones/cyclones.

We emphasize the role of negative thermocline feedback and ocean basin interactions, but further research is needed to investigate the influence of other atmospheric and oceanic processes in affecting the forecasts of ENSO evolution. For example, the meridional shift of wind anomalies could fasten the termination of El Niño events (Lengaigne et al. 2006; McGregor et al. 2013), and the off-equatorial subsurface oceanic process are important for the occurrence of multiyear ENSO events (Iwakiri and Watanabe 2021; Wen et al. 2021).

Our study shows that errors in climatologies and ENSO characteristics in full-field initialized forecasts can be even larger than those in uninitialized simulations of the same model. The initialization imbalance between the "observed" (FOSI) oceanic initial conditions and model dynamics is amplified by coupled feedbacks in the equatorial Pacific, resulting in a stronger cold tongue bias in the forecasts than that inherent to the model. The traditional method of removing the drifting climatology of forecasts cannot eliminate the influence of biased ocean–atmosphere feedbacks on ENSO variability. As a result, these initialized forecasts show ENSO errors that are absent from the uninitialized simulations. For example, the CESM1 forecasts tend to overestimate the duration of ENSO events, while the uninitialized simulations of the same model show realistic proportions of ENSO events lasting one and two years (Wu et al. 2019). It will be interesting to compare ENSO forecast skill in CESM1 with that in its successor, CESM2, which shows a reduced cold tongue bias (Capotondi et al. 2020). More generally, the relationship between mean state biases and ENSO biases warrants further examination using multimodel ensemble forecasts.

Our results reveal opportunities to improve the forecast skill of ENSO events by improving the model's mean state and the accuracy of initial condition data. Despite upgraded physics and spatial resolution across the generations of CMIP models, systematic model errors in tropical Pacific climatology and ENSO variability persist (see a recent review by Guilyardi et al. 2020). The method of "flux adjustment" was adopted as an intermediate step to improve the simulation of the tropical Pacific mean state and its seasonal variation by prescribing a seasonally varying nudging climatology (e.g., Ray et al. 2018). Flux adjustment has been shown to improve the simulation of equatorial Pacific SSTs, ENSO-related climate impacts, and climatological land precipitation (Ferrett and Collins 2019; Johnson et al. 2020; Zhang et al. 2021), while some studies suggest it does not improve the representation of ENSO feedbacks (Spencer et al. 2007; Ferrett and Collins 2019). Another method termed "anomaly initialization" has been used to reduce the model drift and initialization shock, by which forecasts are initialized from the observed anomalies added to the model's climatology. However, it remains unclear and model dependent which initialization method can produce more skillful ENSO and seasonal climate predictions (Magnusson et al. 2013; Smith et al. 2013; Hu et al. 2020). The ocean initial condition data used for our forecasts show errors in reproducing both the climatology and variability of thermocline depth in the equatorial Pacific. These initial conditions are obtained by forcing the ocean model of CESM1 with atmospheric forcing from the reanalysis data and are hence subject to the model errors and uncertainties in the prescribed wind forcing. Integrated efforts aimed at improving model simulations, observing systems and data assimilation methods are needed to make progress on prediction skill of ENSO and its worldwide climate impacts.

Acknowledgments. The authors thank the three anonymous reviewers for constructive comments and suggestions that helped to improve the manuscript. Main observational datasets used in this study are available online: HadISST from the Met Office Hadley Center (http://www.metoffice.gov.uk/hadobs/), BEST from Berkeley Earth (http://berkeleyearth.org/data/), ECMWF Ocean Reanalysis System 4 from ftp://ftp-icdc.cen.uni-hamburg.de/EASYInit/ORA-S4, OAFlux data from the Woods Hole Oceanographic Institution (ftp://ftp.whoi.edu/pub/science/oaflux/data_v3), and NCEP-NCAR reanalysis from https://psl.noaa.gov/data/gridded/data.ncep.reanalysis.html. The CESM1 Large Ensemble simulations are available from https://www.cesm.ucar.edu/projects/community-projects/LENS/. This work is funded by the National Oceanic and Atmospheric Administration (NOAA) Climate Program Office Modeling, Analysis, Predictions, and Projections Program (NA17OAR4310149 and NA17OAR4310145) and the National Science Foundation (NSF) Physical Oceanography Program (OCE-1756883). X. Wu is supported by an Advanced Study Program postdoctoral fellowship from then National Center for Atmospheric Research (NCAR). The CESM project is supported primarily by the NSF. This material is based upon work supported by the NCAR, which is a major facility sponsored by the NSF under Cooperative Agreement 1852977.

REFERENCES

Balmaseda, M., K. Mogensen, and A. T. Weaver, 2013: Evaluation of the ECMWF ocean reanalysis system ORAS4. *Quart. J. Roy. Meteor. Soc.*, **139**, 1132–1161, https://doi.org/10.1002/qj.2063.

Bayr, T., M. Latif, D. Dommenget, C. Wengel, J. Harlaß, and W. Park, 2018: Mean-state dependence of ENSO atmospheric feedbacks in climate models. *Climate Dyn.*, **50**, 3171–3194, https://doi.org/10.1007/s00382-017-3799-2.

——, C. Wengel, M. Latif, D. Dommenget, J. Lübbecke, and W. Park, 2019a: Error compensation of ENSO atmospheric feedbacks in climate models and its influence on simulated ENSO dynamics. *Climate Dyn.*, **53**, 155–172, https://doi.org/10.1007/s00382-018-4575-7.

——, D. I. Domeisen, and C. Wengel, 2019b: The effect of the equatorial Pacific cold SST bias on simulated ENSO teleconnections to the North Pacific and California. *Climate Dyn.*, **53**, 3771–3789, https://doi.org/10.1007/s00382-019-04746-9.

——, A. Drews, M. Latif, and J. Lübbecke, 2021: The interplay of thermodynamics and ocean dynamics during ENSO growth phase. *Climate Dyn.*, **56**, 1681–1697, https://doi.org/10.1007/s00382-020-05552-4.

Behringer, D. W., and Y. Xue, 2004: Evaluation of the global ocean data assimilation system at NCEP: The Pacific Ocean. *Eighth Symp. on Integrated Observing and Assimilation*

Systems for Atmosphere, Oceans, and Land Surface, Seattle, WA, Amer. Meteor. Soc., 2.3, https://ams.confex.com/ams/84Annual/techprogram/paper_70720.htm.

Bellenger, H., E. Guilyardi, J. Leloup, M. Lengaigne, and J. Vialard, 2014: ENSO representation in climate models: From CMIP3 to CMIP5. *Climate Dyn.*, **42**, 1999–2018, https://doi.org/10.1007/s00382-013-1783-z.

Brown, J. N., C. Langlais, and C. Maes, 2014: Zonal structure and variability of the western Pacific dynamic warm pool edge in CMIP5. *Climate Dyn.*, **42**, 3061–3076, https://doi.org/10.1007/s00382-013-1931-5.

Cai, W., and Coauthors, 2019: Pantropical climate interactions. *Science*, **363**, eaav4236, https://doi.org/10.1126/science.aav4236.

Capotondi, A., C. Deser, A. S. Phillips, Y. M. Okumura, and S. M. Larson, 2020: ENSO and Pacific decadal variability in the Community Earth System Model version 2. *J. Adv. Model Earth Syst.*, **12**, e2019MS002022, https://doi.org/10.1029/2019MS002022.

Carton, J. A., and B. S. Giese, 2008: A reanalysis of ocean climate using Simple Ocean Data Assimilation (SODA). *Mon. Wea. Rev.*, **136**, 2999–3017, https://doi.org/10.1175/2007MWR1978.1.

Chang, P., and S. G. Philander, 1994: A coupled ocean–atmosphere instability of relevance to the seasonal cycle. *J. Atmos. Sci.*, **51**, 3627–3648, https://doi.org/10.1175/1520-0469(1994)051<3627:ACOIOR>2.0.CO;2.

——, L. Zhang, R. Saravanan, D. J. Vimont, J. C. Chiang, L. Ji, H. Seidel, and M. K. Tippett, 2007: Pacific meridional mode and El Niño–Southern Oscillation. *Geophys. Res. Lett.*, **34**, L16608, https://doi.org/10.1029/2007GL030302.

Chen, Y.-Y., and F.-F. Jin, 2017: Dynamical diagnostics of the SST annual cycle in the eastern equatorial Pacific: Part II analysis of CMIP5 simulations. *Climate Dyn.*, **49**, 3923–3936, https://doi.org/10.1007/s00382-017-3550-z.

Davey, M. K., and Coauthors, 2002: STOIC: A study of coupled model climatology and variability in tropical ocean regions. *Climate Dyn.*, **18**, 403–420, https://doi.org/10.1007/s00382-001-0188-6.

de Szoeke, S. P., and S.-P. Xie, 2008: The tropical eastern Pacific seasonal cycle: Assessment of errors and mechanisms in IPCC AR4 coupled ocean–atmosphere general circulation models. *J. Climate*, **21**, 2573–2590, https://doi.org/10.1175/2007JCLI1975.1.

DiNezio, P. N., C. Deser, Y. M. Okumura, and A. Karspeck, 2017a: Predictability of 2-year La Niña events in a coupled general circulation model. *Climate Dyn.*, **49**, 4237–4261, https://doi.org/10.1007/s00382-017-3575-3.

——, and Coauthors, 2017b: A 2 year forecast for a 60–80% chance of La Niña in 2017–2018. *Geophys. Res. Lett.*, **44**, 11 624–11 635, https://doi.org/10.1002/2017GL074904.

Ding, H., M. Newman, M. A. Alexander, and A. T. Wittenberg, 2018: Skillful climate forecasts of the tropical Indo-Pacific Ocean using model-analogs. *J. Climate*, **31**, 5437–5459, https://doi.org/10.1175/JCLI-D-17-0661.1.

——, ——, ——, and ——, 2020: Relating CMIP5 model biases to seasonal forecast skill in the tropical Pacific. *Geophys. Res. Lett.*, **47**, e2019GL086765, https://doi.org/10.1029/2019GL086765.

Fang, S.-W., and J.-Y. Yu, 2020: A control of ENSO transition complexity by tropical Pacific mean SSTs through tropical–subtropical interaction. *Geophys. Res. Lett.*, **47**, e2020GL087933, https://doi.org/10.1029/2020GL087933.

Ferrett, S., and M. Collins, 2019: ENSO feedbacks and their relationships with the mean state in a flux adjusted ensemble. *Climate Dyn.*, **52**, 7189–7208, https://doi.org/10.1007/s00382-016-3270-9.

Forget, G., J.-M. Campin, P. Heimbach, C. N. Hill, R. M. Ponte, and C. Wunsch, 2015: ECCO version 4: An integrated framework for non-linear inverse modeling and global ocean state estimation. *Geosci. Model Dev.*, **8**, 3071–3104, https://doi.org/10.5194/gmd-8-3071-2015.

Good, S. A., M. J. Martin, and N. A. Rayner, 2013: EN4: Quality controlled ocean temperature and salinity profiles and monthly objective analyses with uncertainty estimates. *J. Geophys. Res. Oceans*, **118**, 6704–6716, https://doi.org/10.1002/2013JC009067.

Gouretski, V., and F. Reseghetti, 2010: On depth and temperature biases in bathythermograph data: Development of a new correction scheme based on analysis of a global ocean database. *Deep-Sea Res. I*, **57**, 812–833, https://doi.org/10.1016/j.dsr.2010.03.011.

Graham, F. S., A. T. Wittenberg, J. N. Brown, S. J. Marsland, and N. J. Holbrook, 2017: Understanding the double peaked El Niño in coupled GCMs. *Climate Dyn.*, **48**, 2045–2063, https://doi.org/10.1007/s00382-016-3189-1.

Guilyardi, E., A. Capotondi, M. Lengaigne, S. Thual, and A. T. Wittenberg, 2020: ENSO modelling: History, progress and challenges. *El Niño Southern Oscillation in a Changing Climate, Geophys. Monogr.*, Vol. 252, Amer. Geophys. Union, 199–226, https://doi.org/10.1002/9781119548164.ch9.

Ham, Y.-G., and J.-S. Kug, 2011: How well do current climate models simulate two types of El Niño? *Climate Dyn.*, **39**, 383–398, https://doi.org/10.1007/s00382-011-1157-3.

——, S. Schubert, Y. Vikhliaev, and M. J. Suarez, 2014: An assessment of the ENSO forecast skill of GEOS-5 system. *Climate Dyn.*, **43**, 2415–2430, https://doi.org/10.1007/s00382-014-2063-2.

Harris, I., P. D. Jones, T. J. Osborn, and D. H. Lister, 2014: Updated high-resolution grids of monthly climatic observations—The CRU TS3.10 dataset. *Int. J. Climatol.*, **34**, 623–642, https://doi.org/10.1002/joc.3711.

Hu, S., T. Zhou, and B. Wu, 2020: Improved ENSO prediction skill resulting from reduced climate drift in IAP-DecPreS: A comparison of full-field and anomaly initializations. *J. Adv. Model. Earth Syst.*, **12**, e2019MS001759, https://doi.org/10.1029/2019MS001759.

Hunke, E. C., and W. H. Lipscomb, 2008: CICE: The Los Alamos Sea ice model, documentation and software, version 4.0. Los Alamos National Laboratory Tech. Rep. LA-CC-06-012, 76 pp.

Hurrell, J. W., and Coauthors, 2013: The Community Earth System Model: A framework for collaborative research. *Bull. Amer. Meteor. Soc.*, **94**, 1339–1360, https://doi.org/10.1175/BAMS-D-12-00121.1.

Ishii, M., A. Shouji, S. Sugimoto, and T. Matsumoto, 2005: Objective analyses of sea-surface temperature and marine meteorological variables for the 20th century using ICOADS and the Kobe Collection. *Int. J. Climatol.*, **25**, 865–879, https://doi.org/10.1002/joc.1169.

Iwakiri, T., and M. Watanabe, 2021: Mechanisms linking multiyear La Niña with preceding strong El Niño. *Sci. Rep.*, **11**, 17465, https://doi.org/10.1038/s41598-021-96056-6.

Jiang, W., P. Huang, G. Huang, and J. Ying, 2021: Origins of the excessive westward extension of ENSO SST simulated in CMIP5 and CMIP6 models. *J. Climate*, **34**, 2839–2851, https://doi.org/10.1175/JCLI-D-20-0551.1.

Johnson, N. C., L. Krishnamurthy, A. T. Wittenberg, B. Xiang, G. A. Vecchi, S. B. Kapnick, and S. Pascale, 2020: The

impact of sea surface temperature biases on North American precipitation in a high-resolution climate model. *J. Climate*, **33**, 2427–2447, https://doi.org/10.1175/JCLI-D-19-0417.1.

Kalnay, E. M., and Coauthors, 1996: The NCEP/NCAR 40-Year Reanalysis Project. *Bull. Amer. Meteor. Soc.*, **77**, 437–471, https://doi.org/10.1175/1520-0477(1996)077<0437:TNYRP>2.0.CO;2.

Kay, J. E., and Coauthors, 2015: The Community Earth System Model (CESM) large ensemble project: A community resource for studying climate change in the presence of internal climate variability. *Bull. Amer. Meteor. Soc.*, **96**, 1333–1349, https://doi.org/10.1175/BAMS-D-13-00255.1.

Kim, J.-W., and J.-Y. Yu, 2021: Evolution of subtropical Pacific-onset El Niño: How its onset location controls its decay evolution. *Geophys. Res. Lett.*, **48**, e2020GL091345, https://doi.org/10.1029/2020GL091345.

Kim, S., H.-I. Jeong, and F.-F. Jin, 2017: Mean bias in seasonal forecast model and ENSO prediction error. *Sci. Rep.*, **7**, 6029, https://doi.org/10.1038/s41598-017-05221-3.

Kobayashi, S., and Coauthors, 2015: The JRA-55 reanalysis: General specifications and basic characteristics. *J. Meteor. Soc. Japan*, **93**, 5–48, https://doi.org/10.2151/jmsj.2015-001.

Lawrence, D. M., and Coauthors, 2011: Parameterization improvements and functional and structural advances in version 4 of the community land model. *J. Adv. Model. Earth Syst.*, **3**, M03001, https://doi.org/10.1029/2011MS000045.

Lengaigne, M., J.-P. Boulanger, C. Menkes, and H. Spencer, 2006: Influence of the seasonal cycle on the termination of El Niño events in a coupled general circulation model. *J. Climate*, **19**, 1850–1868, https://doi.org/10.1175/JCLI3706.1.

Levitus, S., J. I. Antonov, T. P. Boyer, R. A. Locarnini, H. E. Garcia, and A. V. Mishonov, 2009: Global ocean heat content 1955–2008 in light of recently revealed instrumentation problems. *Geophys. Res. Lett.*, **36**, L07608, https://doi.org/10.1029/2008GL037155.

Li, G., and S.-P. Xie, 2014: Tropical biases in CMIP5 multimodel ensemble: The excessive equatorial Pacific cold tongue and double ITCZ problems. *J. Climate*, **27**, 1765–1780, https://doi.org/10.1175/JCLI-D-13-00337.1.

Lin, J.-L., 2007: The double-ITCZ problem in IPCC AR4 coupled GCMs: Ocean–atmosphere feedback analysis. *J. Climate*, **20**, 4497–4525, https://doi.org/10.1175/JCLI4272.1.

Magnusson, L., M. Alonso-Balmaseda, S. Corti, F. Molteni, and T. Stockdale, 2013: Evaluation of forecast strategies for seasonal and decadal forecasts in presence of systematic model errors. *Climate Dyn.*, **41**, 2393–2409, https://doi.org/10.1007/s00382-012-1599-2.

Manganello, J. V., and B. Huang, 2009: The influence of systematic errors in the southeast Pacific on ENSO variability and prediction in a coupled GCM. *Climate Dyn.*, **32**, 1015–1034, https://doi.org/10.1007/s00382-008-0407-5.

McGregor, S., N. Ramesh, P. Spence, M. H. England, M. J. McPhaden, and A. Santoso, 2013: Meridional movement of wind anomalies during ENSO events and their role in event termination. *Geophys. Res. Lett.*, **40**, 749–754, https://doi.org/10.1002/grl.50136.

Mechoso, C. R., and Coauthors, 1995: The seasonal cycle over the tropical Pacific in coupled ocean–atmosphere general circulation models. *Mon. Wea. Rev.*, **123**, 2825–2838, https://doi.org/10.1175/1520-0493(1995)123<2825:TSCOTT>2.0.CO;2.

Misra, V., L. Marx, M. Fennessy, B. Kirtman, and J. L. Kinter III, 2008: A comparison of climate prediction and simulation over the tropical Pacific. *J. Climate*, **21**, 3601–3611, https://doi.org/10.1175/2008JCLI1932.1.

Mitchell, T. P., and J. M. Wallace, 1992: The annual cycle in equatorial convection and sea surface temperature. *J. Climate*, **5**, 1140–1156, https://doi.org/10.1175/1520-0442(1992)005,1140:TACIEC.2.0.CO;2.

Neale, R. B., and Coauthors, 2012: Description of the NCAR Community Atmosphere Model (CAM 5.0). NCAR Tech. Note NCAR/TN-4861STR, 274 pp., www.cesm.ucar.edu/models/cesm1.0/cam/docs/description/cam5_desc.pdf.

Planton, Y. Y., and Coauthors, 2020: ENSO evaluation in climate models: The CLIVAR 2020 metrics package. *Bull. Amer. Meteor. Soc.*, **102**, E193–E217, https://doi.org/10.1175/BAMS-D-19-0337.1.

Ray, S., A. T. Wittenberg, S. M. Griffies, and F. Zeng, 2018: Understanding the equatorial Pacific cold tongue time-mean heat budget. Part II: Evaluation of the GFDL-FLOR coupled GCM. *J. Climate*, **31**, 9987–10 011, https://doi.org/10.1175/JCLI-D-18-0153.1.

Rayner, N. A., D. E. Parker, E. B. Horton, C. K. Folland, L. V. Alexander, D. P. Rowell, E. C. Kent, and A. Kaplan, 2003: Global analyses of sea surface temperature, sea ice, and night marine air temperature since the late nineteenth century. *J. Geophys. Res.*, **108**, 4407, https://doi.org/10.1029/2002JD002670.

Rohde, R., and Coauthors, 2013: A new estimate of the average Earth surface land temperature spanning 1753 to 2011. *Geoinf. Geostat. Overview*, **1**, 1, https://doi.org/10.4172/2327-4581.1000101.

Schott, F. A., S.-P. Xie, and J. P. McCreary, 2009: Indian Ocean circulation and climate variability. *Rev. Geophys.*, **47**, RG1002, https://doi.org/10.1029/2007RG000245.

Siongco, A. C., H.-Y. Ma, S. A. Klein, S. Xie, A. R. Karspeck, K. Raeder, and J. L. Anderson, 2020: A hindcast approach to diagnosing the equatorial Pacific cold tongue SST bias in CESM1. *J. Climate*, **33**, 1437–1453, https://doi.org/10.1175/JCLI-D-19-0513.1.

Smith, D. M., R. Eade, and H. Pohlmann, 2013: A comparison of full-field and anomaly initialization for seasonal to decadal climate prediction. *Climate Dyn.*, **41**, 3325–3338, https://doi.org/10.1007/s00382-013-1683-2.

Smith, R. D., and Coauthors, 2010: The Parallel Ocean Program (POP) reference manual. Los Alamos National Laboratory Tech. Rep. LAUR-10-01853, 140 pp., https://www.cesm.ucar.edu/models/cesm1.0/pop2/doc/sci/POPRefManual.pdf.

Spencer, H., R. Sutton, and J. M. Slingo, 2007: El Niño in a coupled climate model: Sensitivity to changes in mean state induced by heat flux and wind stress corrections. *J. Climate*, **20**, 2273–2298, https://doi.org/10.1175/JCLI4111.1.

Taschetto, A. S., A. Sen Gupta, N. C. Jourdain, A. Santoso, C. C. Ummenhofer, and M. H. England, 2014: Cold tongue and warm pool ENSO events in CMIP5: Mean state and future projections. *J. Climate*, **27**, 2861–2885, https://doi.org/10.1175/JCLI-D-13-00437.1.

Tippett, M. K., and M. L. L'Heureux, 2020: Low-dimensional representations of Niño 3.4 evolution and the spring persistence barrier. *NPJ Climate Atmos. Sci.*, **3**, 24, https://doi.org/10.1038/s41612-020-0128-y.

Torrence, C., and P. J. Webster, 1998: The annual cycle of persistence in the El Niño–Southern Oscillation statistics. *Quart. J. Roy. Meteor. Soc.*, **124**, 1985–2004, http://dx.doi.org/10.1002/qj.49712455010.

Vannière, B., E. Guilyardi, G. Madec, F. J. Doblas-Reyes, and S. Woolnough, 2013: Using seasonal hindcasts to understand the origin of the equatorial cold tongue bias in CGCMs and its impact on ENSO. *Climate Dyn.*, **40**, 963–981, https://doi.org/10.1007/s00382-012-1429-6.

Vimont, D. J., J. M. Wallace, and D. S. Battisti, 2003: The seasonal footprinting mechanism in the Pacific: Implications for ENSO. *J. Climate*, **16**, 2668–2675, https://doi.org/10.1175/1520-0442(2003)016<2668:TSFMIT>2.0.CO;2.

Wang, B., R. G. Wu, and X. H. Fu, 2000: Pacific–East Asian teleconnection: How does ENSO affect East Asian climate? *J. Climate*, **13**, 1517–1536, https://doi.org/10.1175/1520-0442(2000)013<1517:PEATHD>2.0.CO;2.

Watanabe, M., and F. Jin, 2002: Role of Indian Ocean warming in the development of Philippine Sea anticyclone during ENSO. *Geophys. Res. Lett.*, **29**, 1478, https://doi.org/10.1029/2001GL014318.

Weisberg, R. H., and C. Wang, 1997: A western Pacific oscillator paradigm for the El Niño-Southern Oscillation. *Geophys. Res. Lett.*, **24**, 779–782, https://doi.org/10.1029/97GL00689.

Wen, C., A. Kumar, M. L. Heureux, Y. Xue, and E. Becker, 2021: The importance of central Pacific meridional heat advection to the development of ENSO. *J. Climate*, **34**, 5753–5774, https://doi.org/10.1175/JCLI-D-20-0648.1.

Wengel, C., M. Latif, W. Park, J. Harlaß, and T. Bayr, 2018: Seasonal ENSO phase locking in the Kiel climate model: The importance of the equatorial cold sea surface temperature bias. *Climate Dyn.*, **50**, 901–919, https://doi.org/10.1007/s00382-017-3648-3.

——, ——, ——, ——, and ——, 2019: Eastern equatorial Pacific sea surface temperature annual cycle in the Kiel climate model: Simulation benefits from enhancing atmospheric resolution. *Climate Dyn.*, **52**, 1983–2003, https://doi.org/10.1007/s00382-018-4233-0.

Wittenberg, A. T., A. Rosati, N.-C. Lau, and J. J. Ploshay, 2006: GFDL's CM2 global coupled climate models. Part III: Tropical Pacific climate and ENSO. *J. Climate*, **19**, 698–722, https://doi.org/10.1175/JCLI3631.1.

Wu, R., Z.-Z. Hu, and B. P. Kirtman, 2003: Evolution of ENSO-related rainfall anomalies in East Asia. *J. Climate*, **16**, 3742–3758, https://doi.org/10.1175/1520-0442(2003)016<3742:EOERAI>2.0.CO;2.

Wu, X., Y. M. Okumura, and P. N. DiNezio, 2019: What controls the duration of El Niño and La Niña events? *J. Climate*, **32**, 5941–5965, https://doi.org/10.1175/JCLI-D-18-0681.1.

——, ——, C. Deser, and P. N. DiNezio, 2021a: Two-year dynamical predictions of ENSO event duration during 1954–2015. *J. Climate*, **33**, 4069–4087, https://doi.org/10.1175/JCLI-D-20-0619.1.

——, ——, and P. N. DiNezio, 2021b: Predictability of El Niño duration based on the onset timing. *J. Climate*, **34**, 1351–1366, https://doi.org/10.1175/JCLI-D-19-0963.1.

Xie, S.-P., 1994: On the genesis of the equatorial annual cycle. *J. Climate*, **7**, 2008–2013, https://doi.org/10.1175/1520-0442(1994)007<2008:OTGOTE>2.0.CO;2.

——, and J. A. Carton, 2004: Tropical Atlantic variability: Patterns, mechanisms, and impacts. *Earth Climate: The Ocean-Atmosphere Interaction, Geophys. Monogr*, Vol. 147, Amer. Geophys. Union, 121–142.

Yeager, S., and G. Danabasoglu, 2014: The origins of late-twentieth-century variations in the large-scale North Atlantic circulation. *J. Climate*, **27**, 3222–3247, https://doi.org/10.1175/JCLI-D-13-00125.1.

Yeager, S. G., A. Karspeck, and G. Danabasoglu, 2015: Predicted slowdown in the rate of Atlantic sea ice loss. *Geophys. Res. Lett.*, **42**, 10 704–10 713, https://doi.org/10.1002/2015GL065364.

——, and Coauthors, 2018: Predicting near-term changes in the Earth system: A large ensemble of initialized decadal prediction simulations using the Community Earth System Model. *Bull. Amer. Meteor. Soc.*, **99**, 1867–1886, https://doi.org/10.1175/BAMS-D-17-0098.1.

Yu, L., and R. A. Weller, 2007: Objectively analyzed air–sea heat fluxes for the global ice-free oceans (1981–2005). *Bull. Amer. Meteor. Soc.*, **88**, 527–540, https://doi.org/10.1175/BAMS-88-4-527.

Zhang, H., R. Seager, J. He, H. Diao, and S. Pascale, 2021: Quantifying atmosphere and ocean origins of North American precipitation variability. *Climate Dyn.*, **56**, 4051–4074, https://doi.org/10.1007/s00382-021-05685-0.

Zheng, Y., J. Lin, and T. Shinoda, 2012: The equatorial Pacific cold tongue simulated by IPCC AR4 coupled GCMs: Upper ocean heat budget and feedback analysis. *J. Geophys. Res.*, **117**, C05024, https://doi.org/10.1029/2011JC007746.